The grand rotation curve of the Milky Way from the central black hole to dark halo

Yoshiaki Sofue[1*]

[1*]Institute of Astronomy, The University of Tokyo, Osawa 2-21-1, Mitaka, 183-0015, Tokyo, Japan .

Corresponding author(s). E-mail(s): sofue@ioa.s.u-tokyo.ac.jp;

Abstract

We update the grand rotation curve of the Milky Way to that with the highest spatial and velocity resolutions and the most complete sampling from the central supermassive black hole to the outermost dark halo, up to $\sim$ **300** kpc. The new RC, named GRC27, is presented in the form of figures and ascii-formatted tables for wider usage for the Galactic dynamics. The shape of the new RC confirms the current RC, and is ascribed by the following five components: 1. The central Keplerian curve due to the supermassive black hole at the nucleus; 2. A core component of radius $\sim$ **2.3** pc attributed to either a high-density concentration of mass $\sim 2.3\times10^7 M_\odot$ or a non-circular motion in the inner-most bar potential. 3. A bulge component with a high velocity peak at a radius of $\sim$ **160** pc, which can be attributed to a bulge of mass $\sim 1.1\times10^{10} M_\odot$ or to an eccentric gas flow in a bar. 4. An exponential disk of scale radius $\sim$ **3.9** kpc and mass $\sim 0.86\times10^{11} M_\odot$; and 5. A dark matter halo fitted by the NFW (Navarro-Frenk-White) model with a scale radius $h\sim$ **14 kpc** and enclosed mass $M(\leq h)\sim 1.7\times10^{11} M_\odot$, which leads to a lower limit to the local DM density at Sun of $\rho_\odot^{\rm DM}\sim$ **0.21** GeV cm^{-3} . The Einasto model with an exponent index $n\sim$ **5** can also fit the observed RC to a good agreement with NFW, while smaller index of $n\lesssim$ **4** is excluded.

Keywords: galaxies: individual (Milky Way) — galaxies: kinematics and dynamics — Galaxy: kinematics and dynamics — Galaxy: structure — dark matter

1 Introduction

The rotation curve (RC) is the most fundamental tool for measuring the dynamical mass, including dark matter, and its distribution in galaxies under the assumption that a galaxy is rotating around the polar axis (Sofue and Rubin, 2001; Sofue, 2017, 2020; Lelli et al., 2016; McGaugh, 2016; Salucci, 2019). In our earlier papers (Sofue et al., 2009; Sofue, 2012, 2013), we constructed a grand RC (GRC) of the Galaxy from the nucleus to halfway to M31, including the outer halo, by combining the existing rotation data from the 1980s to the 2000s. We have deconvolved the GRC into several mass components to obtain fundamental parameters such as the total mass and scale size of each component, as well as the local density of dark matter (DM) (Sofue, 2013, 2020).

As an alternative and complementary approach to the dynamical method, extensive photometric determinations, particularly in infrared wavelengths, have revealed the luminous mass distribution in the inner Galaxy and the detailed distribution of stellar components, including the nuclear disk, bulge and/or bar, and the inner disk (Schödel et al., 2014; Robin et al., 2012, 2014; Wegg et al., 2015; Portail et al., 2015; Ness & Lang, 2016; Valenti et al., 2016; Simion et al., 2017; Marasco et al., 2025), while the dark matter mass, and hence the total mass, has been excluded from the photometric approach.

In this paper, we revise the current RCs of the Milky Way by employing the most recent data about Galactic rotation and present a new unified rotation curve. In order to avoid confusion with the "universal RC (URC)" for galaxies (Salucci, 2019), we call our RC from the nucleus to halo of the Milky Way the 'grand RC (RC) (GRC27)'.

We integrate the current RCs determined individually for the Galactic Center by the ALMA molecular line survey of the central molecular zone (CMZ) (Sofue et al., 2025), the inner disk using the CO and HI-line surveys of the Galactic plane (Sofue & Kohno, 2025), the stellar disk by trigonometry of maser sources using VERA (VERA Collaboration et al., 2020) and VLBA

(Reid et al., 2019), the disk stars by GAIA (Eilers et al., 2019; Zhou et al., 2023; Ou et al., 2024), and 3D velocities of globular clusters and dwarf galaxies with GAIA (Jiao et al., 2023; Sylos Labini, 2024).

However, we do not use the earlier RCs derived from HI and CO observations of the gas disk of the outer Galaxy outside the Solar circle, where the gaseous RC is claimed to be distinct from the stellar RC (Nelson et al., 2026). We adopt the Galactic constants $R_0 = 8.18$ kpc (Gravity Collaboration et al., 2019) and $\Theta_0 = 235.1$ km s^{-1} (Sofue & Kohno, 2025).

The main objective of this paper is to construct and present the updated GRC (unified rotation curve) at the highest resolution, highest sampling rate, and widest radius range. This curve provides the most fundamental observational kinematic constraints for galactic dynamical models and will be useful for broader applications, such as determining mass distributions and evaluating the reliability of simulation models. As for one possibility, we have decomposed the GRC into multiple components and calculated the masses and scale radii, assuming their motions are circular.

2 Construction of a new GRC

We integrate the partially determined rotation curves in specific radii based on the most recent observations. Below, we describe the data.

2.1 Central black hole

The rotation curve around the central supermassive black hole (SMBH) located at the nucleus (Sgr A*) with a mass of $M_1 = 4.3 \times 10^6 M_\odot$ (GRAVITY Collaboration et al., 2022) is represented by the Keplerian law, as shown in figure 3 (A).

2.2 Central Molecular Zone (CMZ)

We have recently determined the RC in the CMZ using the ACES (ALMA CMZ Exploration Survey) data (Longmore et al., 2026) by applying the terminal velocity method to the longitude-velocity diagrams (LVD) of the CS ($J = 2-1$)-line emission from the molecular gas in the CMZ and the H40α-line from the ionized gas in the minispiral (Sofue et al., 2025). The entire CMZ has a nearly flat RC at $V \sim 100$ km s^{-1} associated with a peak around $R \sim 5$ pc. The innermost V within $R \lesssim 1$ pc increases toward the nucleus, obeying the Keplerian law due to the central SMBH.

2.3 Gas disk inside the solar circle by terminal velocities of CO and HI lines

Inside the solar circle ($-90° \leq l \leq 90°$), the rotation velocity $V(R)$ at the galacto-centric distance $R = R_0 \sin\ l$ is calculated simply by correcting the terminal velocity $V_{\rm term}$ for the circular motion of the LSR (local standard of rest) at the Sun:

$$V(R) = V_{\rm term} + \Theta_0 \ \sin\ l. \qquad (1)$$

In figure 3 we show the inner RC obtained recently by Sofue & Kohno (2025), applying TVM to CO and HI line survey data of the Galactic plane (Dame et al., 2001; HI4PI Collaboration et al., 2016; Umemoto et al. , 2017; Braiding et al., 2015; Cubuk et al., 2023).

2.4 Stellar disk by VLBI trigonometry of maser sources

Trigonometric measurements of maser sources using VERA (VLBI exploration of radio astrometry) (VERA Collaboration et al., 2020) and VLBA (very long baseline array) (Reid et al., 2019) have provided accurate 3D motions of the sources in the Galactic disk, which yielded rotation curves at high accuracy. These results were combined with the inner rotation curve from the terminal velocity to yield a rotation curve from the Galactic Center to the halo at $R \sim 15$ kpc. We include the rotation velocities of maser sources from VERA and VLBA measurements for the disk RC by taking running averages with our inner RC (Sofue & Kohno, 2025). In this work, we do not use the gaseous rotation curve outside the Solar circle from CO and HI-line observations, which is claimed to be displaced from the Virial motion in the Galactic potential (Nelson et al., 2026).

2.5 Stellar disk and halo by GAIA astrometry

The GAIA mission has provided proper motions of billions of stars in the Milky Way and yielded high accuracy rotation curves of the mid to outer Galactic disk at $R \sim 8$ to 25 kpc (Eilers et al., 2019; Jiao et al., 2023; Sylos Labini, 2024). We also include their rotation curve by taking running averages with the RC for the disk described above. Bird et al. (2022) presents circular velocities from $R \sim 10$ to ~ 70 kpc using sophisticated analysis. Although their plot is in agreement with our plot, it is more scattered, and the data list is not available, so we do not employ it.

2.6 Halo RC from 25 to 100 kpc by globular clusters

For the outer Galactic halo, we employ GAIA astrometry of globular clusters (Vasiliev & Baumgardt, 2021; Wang et al., 2022). In figure 4 we plot the rotation velocities presented by Wang et al. (2022), which cover $R \sim 25$ to ~ 100 kpc.

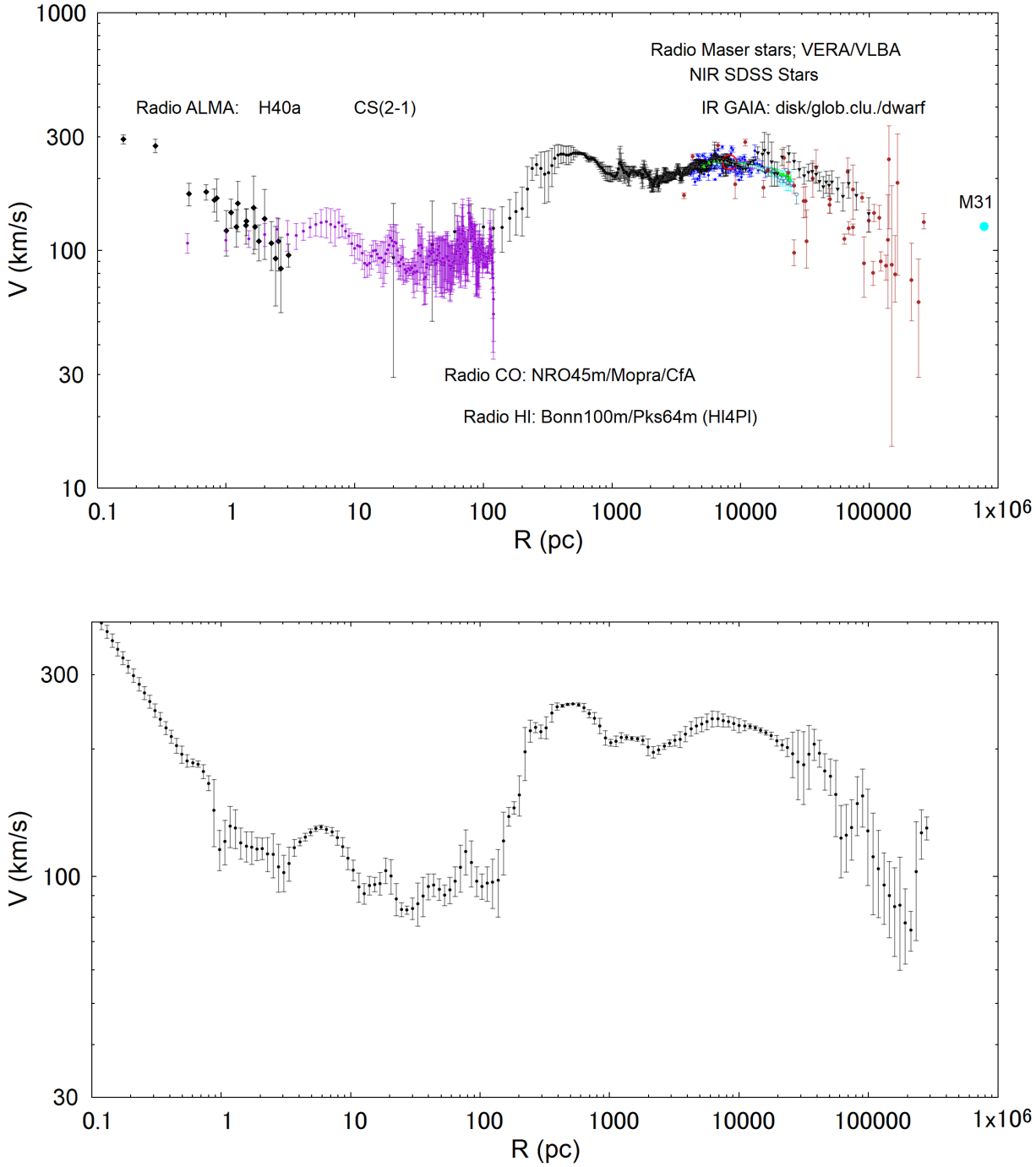


Fig. 1 [Top] RC data from the literature (Sofue & Kohno, 2025; VERA Collaboration et al., 2020; Reid et al., 2019; Eilers et al., 2019; Jiao et al., 2023; Sylos Labini, 2024; Huang et al., 2016; Li et al., 2021; Zhou et al., 2023; Ou et al., 2024). Further details about literature are given in the text and captions for figures 2-3. The big dot marks the Sun at (8.2 kpc, 235 km s^{-1}). The outermost blue dot marks M31 for $V = V_{3D}/\sqrt{2}$ with $V_{3D} \sim 178$ km s^{-1} is the Galacto-centric 3D velocity of M31 (Salomon et al., 2016). [Bottom] Same, but running averaged with a radial increment 0.1 dex combined with a Keplerian curve for the central BH of mass $4.3 \times 10^6 M_\odot$. Ascii formatted table of this figure is given in Appendix. Alt text: Rotation curve data of the Galaxy.

2.7 Halo RC from 25 to 300 kpc by dwarf galaxies

For $\sim$ 25 to 300 kpc we use the 3D velocities dwarf galaxies observed by GAIA (Li et al., 2017, 2021; Hammer et al., 2021, 2023). Following Sofue (2013) we introduce a "pseudo" rotation velocity of dwarf galaxies defined by

$$V = \eta V_{3D} = \eta \sqrt{v_{\rm RA}^2 + v_{\rm Dec}^2 + v_{\rm radial}^2}. \qquad (2)$$

Here, v_i (i = RA, Dec, radial) are the velocities calculated for the proper motions and radial velocity with

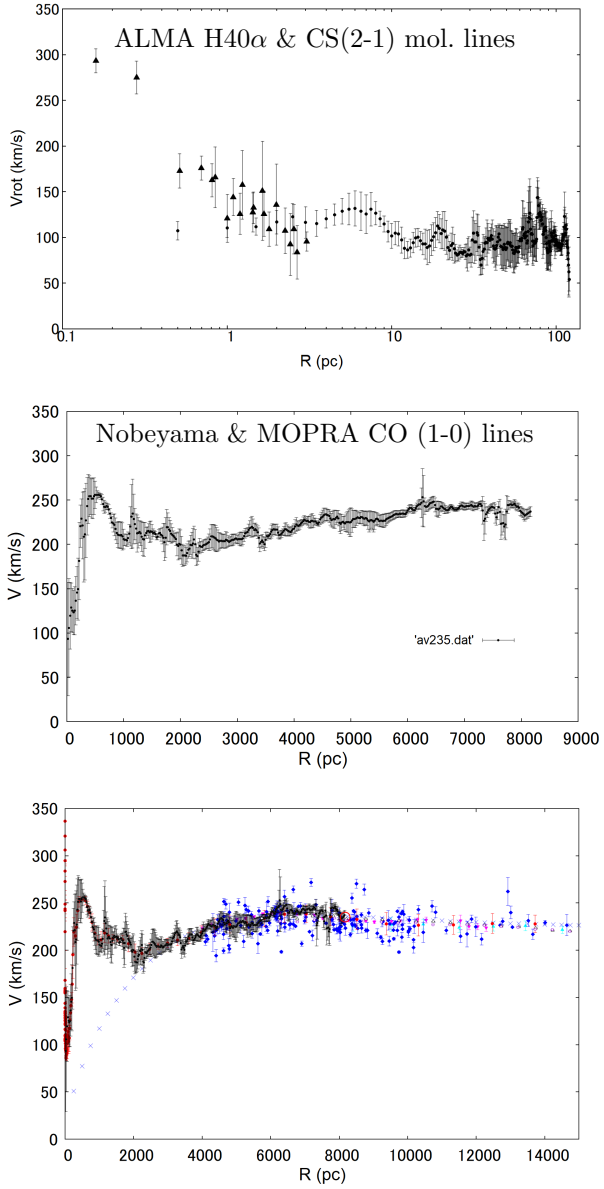


Fig. 2 [Top] Terminal velocity RC of the CMZ in the central 120 pc obtained by H40α (triangles) and CS ($J = 2 - 1$) (dots) lines in semilogarithmic scaling (Sofue et al., 2025). [Middle] Terminal-velocity RC using CO-line LVD from Nobeyama 45-m FUGIN and Mopra. [Bottom] Terminal velocity RCs in the inner Milky Way using CO-line position-velocity diagrams (black dots, red dots) (Sofue & Kohno, 2025) compared with the circular velocities derived from VERA (blue diamonds) (VERA Collaboration et al., 2020) , VLBA (inverse triangles, large cross) (Reid et al., 2019), and Gaia (cyan and violet triangles) (Eilers et al., 2019; Jiao et al., 2023; Sylos Labini, 2024; Zhou et al., 2023; Ou et al., 2024). Alt text: Rotation curve of the Galactic Center.

GAIA, and η is a conversion factor for the 3D velocity to a pseudo circular velocity at the same radius. We assume $\eta \sim 1/\sqrt{2}$, considering that the dwarfs are halfway to their apocenters and the orbital inclinations to the line of sight are random. Using the velocities thus converted, we perform the Gaussian running average and plot them in figure 4. The η correction could vary between $\eta \sim 1$ and $\sim 1/\sqrt{3}$, depending on the dynamical condition of the halo. This means that the dark halo mass estimation in this paper includes a systematic error of a factor of ~ 2.

2.8 GRC27: Unified RC from the GC to outermost halo

We then construct a unified RC (URC) by taking the Gaussian running average (GRA) of the rotation velocities $V(R_i)$ measured at $R = R_i$ for the i-th data point by the individual methods. The GRA value of V at a radius R is calculated by

$$V(R) = \Sigma_{i=1}^{N} V_i w_i \ / \ \Sigma_{i=1}^{N} w_i \tag{3}$$

and

$$\delta V = \left[\Sigma (V(R) - V_i)^2 w_i \ / \ \Sigma w_i\right]^{1/2}, \tag{4}$$

where

$$w_i = \exp\left[-(R_i - R)^2 \ / \ \delta R^2\right] \sigma_i^{-2}, \tag{5}$$

and σ_i is the error of the observed value of the i-th data point, and $\delta R \sim 0.1R$ is the smoothing width. We plotted the GRC in figure 4 at the same logarithmic radius interval and listed the calculated values in tables 2 — ?? in the appendix.

Figure 3 shows the obtained results with different scalings from the central region to the halo. Figure 4 shows a simultaneous plot of the RC that includes the SMBH, CMZ, bulge, disk, halo, and outer halo up to $\sim$ 300 kpc, about halfway to the Andromeda galaxy, in semi-logarithmic and logarithmic scaling. We name this RC the "GRC27" (unified rotation curve 2026).

3 Deconvolution of GRC into 5 components

The major purpose of this paper was to present the newly constructed unified rotation curve of the Milky Way shown in figures 4 and 4, referred to as GRC27. This rotation curve is sampled at the highest spatial resolution ever obtained, as well as the highest velocity resolution inside the solar circle, based on the accurate analysis of the highest resolution molecular line cube data of the Galactic disk using the terminal velocity method. It further combines the most recent proper motion data of globular clusters and dwarf galaxies. Thus, GRC27 has achieved sufficiently tight logarithmic as well as semi-logarithmic plots of the rotation velocities, covering the widest area of the Galaxy from the central supermassive black hole to the dark matter halo at radii of approximately 300 kpc, almost halfway to the neighboring major member of the Local Group, M31. The curve is useful for a variety of analyzes of Galactic structure and dynamics, and the obtained values are listed in table 2 in the Appendix.

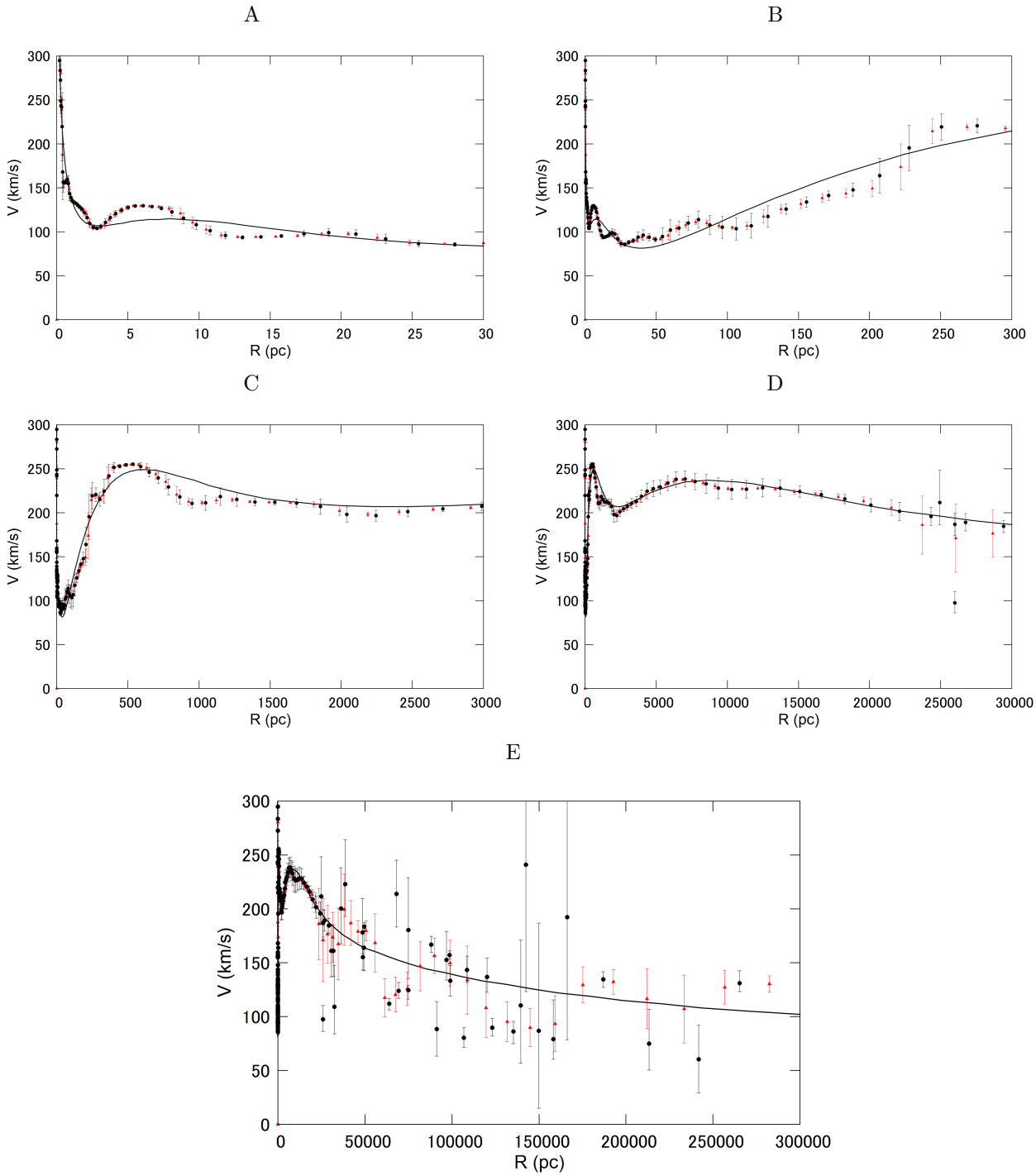


Fig. 3 [A] GRC in the central 10 pc; [B] 0 to 100 pc; [C] 0 to 1 kpc; [D] 0 to 10 kpc; [E] 0 to 100 kpc; and [F] 0 to 1 Mpc. The GRC was constructed by combining the innermost RC shown in figure 2, the inner RC of the gas disk using the terminal velocity method (black dots) (Sofue & Kohno, 2025), trigonometry of maser sources with VERA (blue dots) (VERA Collaboration et al., 2020) and VLBA (magenta dots) (Reid et al., 2019), disk stars by GAIA DR3 (brown triangles) (Jiao et al., 2023), GAIA trigonometric rotation curves of globular clusters (Eadie & Jurić, 2019; Vasiliev & Baumgardt, 2021; Wang et al., 2022), and GAIA proper motions of dwarf galaxies for $\eta = 1/\sqrt{2}$ (Li et al., 2021; Hammer et al., 2021, 2023). The innermost Keplerian curve represents the SMBH of $4 \times 10^6 M_\odot$ (GRAVITY Collaboration et al., 2022). Alt text: GRC27.

3.1 RC deconvolution assuming circular rotation

One of the applications of rotation curves is the derivation of mass distribution, assuming circular rotation. However, this assumption is not fully plausible in the inner Milky Way, where a bar potential may control the dynamics. We will discuss the limitations and systematics of this method in section 4.

Widely adopted models to represent the bulge and disk are the exponential sphere, exponential disk, Sérsic type potential, Miyamoto-Nagai potential, and the Plummer potential. We adopt the exponential

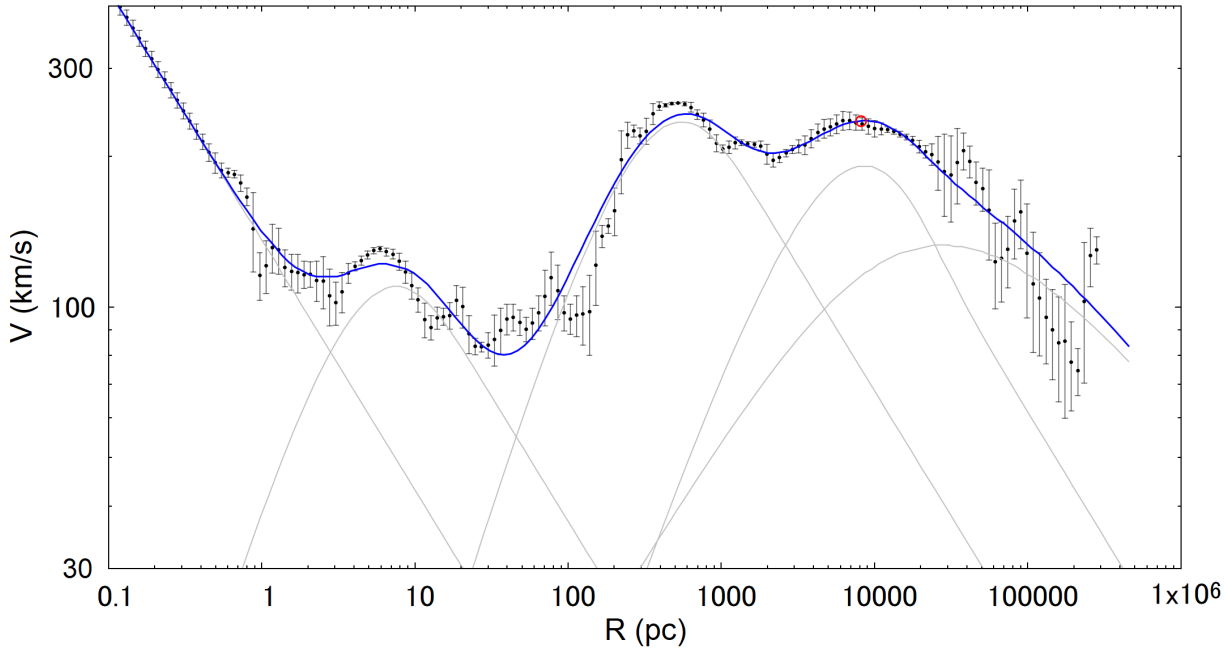


Fig. 4 GRC27 deconvolved into SMBH (component 1), core (component 2), bulge (3), disk (4) and dark halo (5). Alt text: Unified rotation curve from the GC to halo.

sphere for the core and bulge and a flat exponential disk for the disk component. We note that all these density models yield similar rotation velocities due to the long range force of gravity, composed of a rigid-body rise, a peak at $\sim 2a$ (a =scale radii), and a Keplerian decrease, coinciding within a few percent. Note that $\exp(-x/a) = \exp(-x/2a)^2 \sim \mathrm{sech}(x/a) \sim \mathrm{sech}^2(x/2a)$, and $\mathrm{sech}^2(x/a^*)$ ($a^* = 2a$) is often used in other works. The Einasto model is categorized in the exponential sphere, as will be discussed in more detail later. However, NFW type potentials for the dark halo behave quite differently, diverging outward because of the slow decrease in density.

The rotation curve is represented by a superposition of N dynamical mass components as

$$V(R) = \sqrt{\Sigma_{i=1}^{N} V_i(R)^2}, \tag{6}$$

where $V_i(R)$ is the rotation velocity at radius R due to the i-th component. By closely examining GRC27 in figure 4, we recognize five ($N = 5$) distinct mass components characterized by five velocity peaks at the center ($R \sim 0$ pc), $R \sim 5$ pc, ~ 500 pc, ~ 5000 pc, and an outskirt that extends to $R \sim 300$ kpc. We attribute these peaks to 1) SMBH, 2) core, 3) bulge, 4) disk, and 5) dark halo, and try to fit GRC27 by superposing these mass components employing the following profiles. We then decompose the observed RC into the five components by the least-χ^2 method using the following functions representing the individual components. The fitted parameters are listed in table 1

3.1.1 Supermassive black hole

The innermost rotation curve at $R \lesssim 1$ pc is represented by the Keplerian law for the massive black hole with $M_{\rm BH} = 4.3 \times 10^6 M_\odot$ (GRAVITY Collaboration et al., 2022):

$$\phi = GM_1/R, \tag{7}$$

and

$$V(R) = V_1/\sqrt{R/a_1} \tag{8}$$

with $V_1 = 136.6$ km s^{-1}and $a_1 = 1$ pc.

3.1.2 Core and bulge by exponential spheres

For the core component, we adopt a spherical exponential density profile expressed as

$$\rho_i(R) = \rho_0^i \exp(-R/a_i), \tag{9}$$

where ρ_0^i and a_i are the central density and scale radius of the i-th mass component. The rotation velocity is calculated by

$$V_i(R) = \sqrt{GM_i(R)/R}, \tag{10}$$

where

$$M_i(R) = \int_0^R \rho_i(r) 4\pi r^2 dr \tag{11}$$

is the enclosed mass inside R. We stress that, because gravity has a long range force, the exponential potential is a good approximation to that of a Plummer potential, as well as any similar mass concentrations with sufficiently rapid density decrease, with an accuracy of a few percent (Sofue, 2017). By fitting to the

URC, we obtain the scale radius and mass for the core to be $a_2 \simeq 2.3$ pc and $M_2 \simeq 3.3 \times 10^7 M_\odot$.

We adopt the same form for the bulge component. The fitting leads to $a_3 \simeq 162$ pc and $M_3 \simeq 1.1 \times 10^{10} M_\odot$, which is nearly identical to the fit using the $\mathrm{sech}^2(R/a^*)$ function with $a_3^* \sim 2a_3 \sim 0.32$ kpc.

However, the inner Galaxy has a bar, and the bar-driven non-circular motion of the gas does not necessarily represent the true mass distribution. This issue will be discussed in section 4 in details.

3.1.3 Exponential flat disk

The galactic disk is represented by an exponential disk (Freeman, 1970), where the surface mass density (SMD) is expressed as

$$\Sigma_4(R) = \Sigma_0 \exp(-R/a_4). \tag{12}$$

Here, Σ_0 is the central value, a_4 is the scale radius, and R is the radius inside the Galactic plane. The total mass of the exponential disk is given by $M_4 = 2\pi\Sigma_0 a_4^2$. The rotation velocity is expressed by

$$V_4(R) = V_0 \sqrt{y^2[I_0(y)K_0(y) - I_1(y)K_1(y)]}, \tag{13}$$

where

$$V_0 = \sqrt{4\pi G \Sigma_0 a_4} = \sqrt{2GM_4/a_4} \tag{14}$$

with $y = R/(2a_4)$, I_i, and K_i as the modified Bessel functions. By fitting, we obtain the disk radius and total disk mass to be $a_4 \simeq 3.9$ kpc and $M_4 \simeq 0.86 \times 10^{11} M_\odot$.

3.1.4 Dark halo by NFW model

The extended outskirts of the GRC beyond $R \sim 15$ kpc can be fitted by the dark halo represented by the NFW (Navaro-Frenk-White) density profile (Navarro et al., 1997),

$$\rho_5(x) = \frac{\rho_0}{x(1+x)^2}, \tag{15}$$

where $x = R/h$ and $h = a_5$ are the scale radii. The rotation velocity is given by

$$V_5(R) = \sqrt{GM_5(R)/R}, \tag{16}$$

and the mass inside R is given by

$$M_5(R) = 4\pi\rho_0 h^3[\ln(1+x) - x/(1+x)]. \tag{17}$$

By this function, the halo mass diverges with increasing radius, so no definite total mass can be calculated from the fitting. Instead, we calculated a mass enclosed in the fitted scale radius $h_5 \simeq 14$ kpc to be $M_5 \sim 2.5 \times 10^{11} M_\odot$, as listed in table 1. Further detail about halo mass will be described in section 3.2.

Table 1 Fitting parameters of the GRC27 for $\eta = 1/\sqrt{2}$.

Component	a_i(pc)	$M_i(M_\odot)$
2	2.23 ± 0.07	0.321E+08 ±.109E+07
3	163.17 ± 1.80	0.107E+11 ±.157E+09
4	3989.52 ± 73.77	0.874E+11 ±.214E+10
5	12928.35 ± 445.93	0.244E+12 ±.905E+10

3.1.5 Dark halo by Einasto model

The Einasto density profile (Einasto, 1965; Retana-Montenegro et al., 2012) can be used to represent the halo, which has the following form:

$$\rho_{\mathrm{E}} = \rho_6 \exp\left[-\left(\frac{r}{a_6}\right)^{\frac{1}{n}}\right], \tag{18}$$

where ρ_6, a_6 and n are constants. This model is essentially the same as the exponential sphere model, except for the mildness of the shape near the peak: RC increases linearly at $r \ll a_6$, attains a maximum at $\sim 2a_6$, and declines outward, following the Keplerian law at large radius as

$$V_{\mathrm{Einasto}} \propto r^{-1/2}. \tag{19}$$

The outer behavior contrasts to the milder decrease of the NFW curve as

$$V_{\mathrm{NFW}} \propto (\ln r/r)^{-1/2}. \tag{20}$$

The Einasto model contains three independent parameters: the central density ρ_6, scale radius a_6 and the exponent index n. Therefore, it is practically impossible to apply the least χ^2 fitting to our data, although it might be possible if we had a dataset with sufficiently accurate and tight sampling. Here, we only attempt an eye fitting for the halo region by overlaying circular velocity curves calculated for the Einasto density profile with $n = 1$–6 on the outer part of figure 4, where the peak positions are adjusted to coincide with the peak of the NFW curve. We find that the Einasto curve with $n = 5$ resembles the NFW curve, suggesting that it also fits GRC27 reasonably. However, we may be able to exclude the cases with $n \lesssim 4$, which decline too quickly beyond ~ 200 kpc.

A meaningful difference between the two models will appear if further observational points are available at larger radii of $R \gtrsim 600$ kpc, far beyond half the distance to M31 at 780 kpc. This means that there is no way to distinguish between the two models using the current RC data of the Milky Way.

3.2 Mass distribution

The least χ^2 fitting results using these functions are summarized in table 1. The rotation velocity was calculated using the fitted parameters and plotted in Figure 4. The calculated RC reproduces GRC27 from the center to $R \sim 30$ kpc well, and the outer halo (up

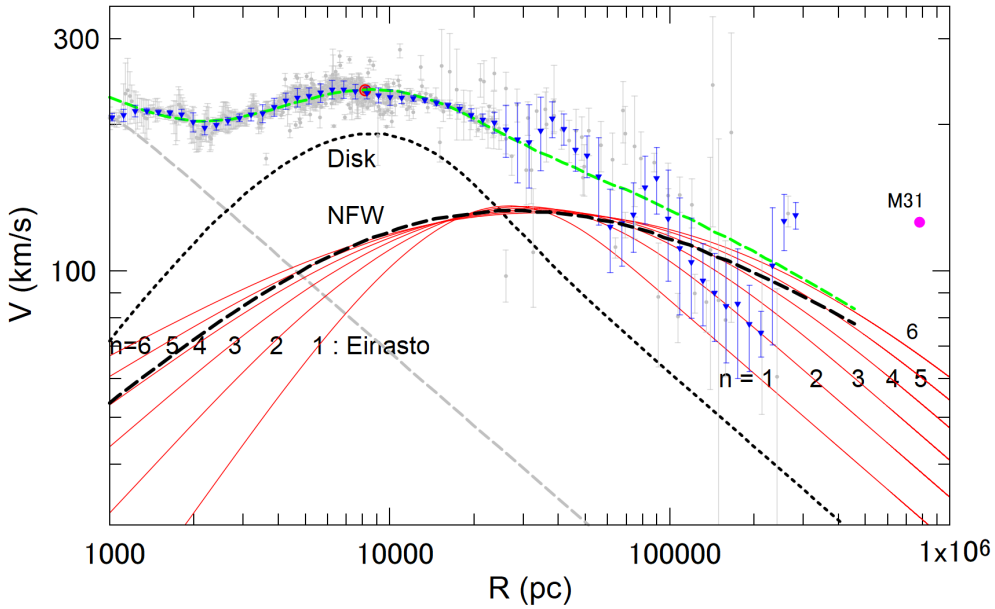


Fig. 5 Comparison of the result with the Einasto model for $n = 1 - 6$. The Einasto model with $n \sim 5$ is almost identical with NFW at $R \gtrsim 10$ kpc. Alt text: Comparison with Einasto model.

to 300 kpc) also shows a reasonable fit within the margin of error. GRC27 demonstrates the existence of a massive halo in the outermost region up to $R \sim 300$ kpc, which can be reasonably represented by the NFW mass model. However, GRC27 does not support the Keplerian decrease in rotation velocity at $R \gtrsim 25$ kpc.

Using dynamically fitted parameters, the density distribution and cumulative mass were calculated as a function of R and plotted in Figure 6. This diagram shows that mass is concentrated at a high density over a range of more than 10 orders of magnitude, from the dark halo to the nucleus.

Using figure 6, we obtain the critical radius and mass of the Galaxy to be $R_{200} \sim 82$ kpc at which the mass density becomes equal to the cosmological critical density, $\rho_{200} = 200 \times (3H_0^2)/(8\pi G) = 1.9 \times 10^{-27}$g cm^{-3} $= 2.8 \times 10^{-5} M_\odot$pc^{-3} with $H_0 = 71$ km s^{-1}Mpc^{-1} being the Hubble constant. The critical total mass (halo + disk) is obtained as $M_{200} = M(R_{200}) \sim 4 \times 10^{11} M_\odot$.

An alternative "total mass" of the Galaxy may be defined as the enclosed mass inside halfway, $R_{1/2} \sim$ 390kpc, to the neighboring giant galaxy M31 at $R_{\rm M31} = 780$ kpc. Using the fitting curve to the GRC27, we have $V(390$ kpc$) \sim 90$ km s^{-1} , so that we obtain $M_{390\ \rm kpc} \sim 7.3 \times 10^{11} M_\odot$. Within this half radius to M31, the bulge+disk ($\sim 0.96 \times 10^{11} M_\odot$) shares $\sim 13\%$ and the dark matter shares $\sim 87\%$ of the total Galaxy mass.

3.3 Local DM density

The local density of DM is a key parameter for the direct detection experiments of DM. Using figure 6 (equation 15) we obtain the local density of DM at the Sun due to the dark halo alone to be $\rho_\odot^{\rm DM} \sim 5.7 \times 10^{-3} M_\odot$pc$^{-3} \simeq 0.21$ GeV cm^{-3} . Note that this is a lower limit of the DM density near the Sun: it represents the dark halo contribution alone, not including the DM in the disk, which has twice the density of DM near the Sun. Separation and more precise determination of the stellar and DM masses inside the disk is beyond this work, and the readers may refer to a more advanced study about this problem (Iocco et al., 2015)

3.4 Scaling relation

Deconvolution of the GRC into multiple components enables us to examine the scaling relation between the scale radius, a_i, and total mass, M_i, among the SMBH, core, bulge, disk, and dark halo. For the BH, we define the scale radius as the radius at which the gravity of the BH dominates that of the core component, i.e., $a_{\rm BH} \sim 0.5$ pc. Figure 7 shows the total masses thus derived against the scale radii of the five components. We find a linear proportionality between the radius and the total mass, which varies by more than six orders of magnitude and is expressed by $M \sim 10^7 M_\odot (R/1\ {\rm pc})^{1.1}$, as shown by the straight line in the figure. The diagram may provide a scaling relation within an individual galaxy about the coevolution of the BH, bulge, disk, and dark halo. This provides a complementary relation to the scaling law between the masses of the BHs and bulges among different galaxies (Kormendy & Ho, 2013).

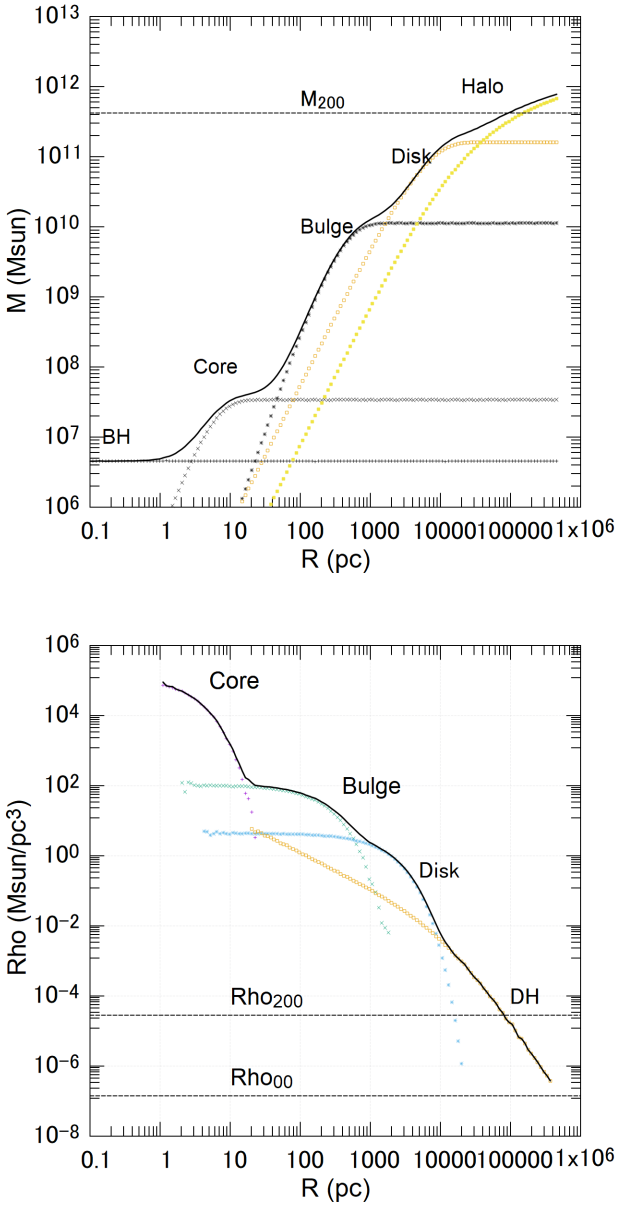


Fig. 6 [Top] Cumulative mass $M(R)$ calculated for the parameters determined by the least-χ^2 fitting to URC. [Bottom] Volume density calculated for the fitted URC. Alt text: Cumulative mass and density distributions.

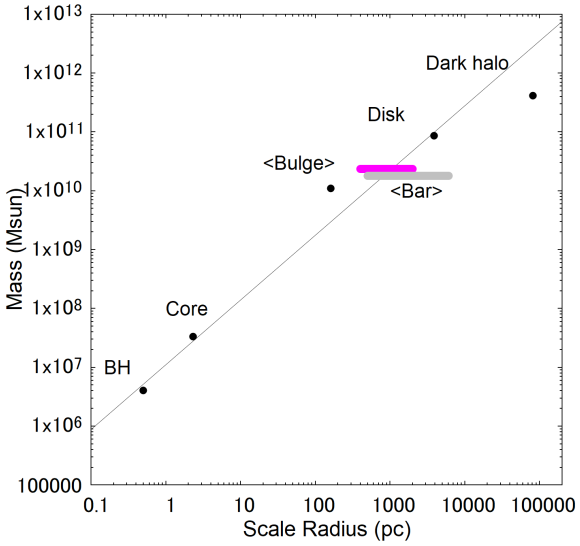


Fig. 7 Scale radius vs total mass of the five mass components of the Milky Way. The radius for BH is approximated by its 'gravity dominant radius'. Instead of the bulge, we may adopt photometric bar (Simion et al., 2017) (magenta thick line) or a dynamical model (Hunter et al., 2024) (grey thick line). The DH represent $M_{200}^{\rm DM}$ (DH component alone). The thin straight line indicates $M = 10^7 (R/1{\rm pc})^{1.1} M_\odot$. Alt text: Scaling relation among the deconvolved mass components.

4 Discussion

4.1 Consistency with photometric results

Extensive photometric observations in infrared wavelengths at ~ 2 to $\sim 4\mu$m have been obtained of the central stellar component (Schödel et al., 2014), the bulge, and the inner disk (Robin et al., 2012, 2014; Wegg et al., 2015; Portail et al., 2015; Ness & Lang, 2016; Valenti et al., 2016; Simion et al., 2017; Marasco et al., 2025). Our results for the scale radii and masses of the core, bulge, and disk are consistent with these results within a factor of 1.5 to 2.

The photometric scale radius and mass of the central stellar cluster, $a_2 \simeq 4$ pc and $M_2 \sim 4 \times 10^7 M_\odot$, from the infrared photometry (Schödel et al., 2014) are close to the present dynamical values $a_2 \sim 2.3$ pc and $M_2 \sim 3.3 \times 10^7 M_\odot$ (table 1).

The scale radius of the central bulge or a bar inferred from infrared photometry of $a_3^* \sim 2a_3 \sim 0.4 - 2$ kpc (Simion et al., 2017) is larger than the dynamical fitting value of $2a_3 = a_3^* \sim 0.3$ kpc. The photometric mass $\sim 1.8 - 2.4 \times 10^{10} M_\odot$ is also about twice the dynamical mass of $M_3 \sim 1.1 \times 10^{10} M_\odot$ for the assumed spherical bulge. The difference may be either that the RC does not manifest the true mass due to non-circular motion, or that the photometry misses the true mass because it lacks measurements of the brightest region in the galactic plane at $|b| \lesssim 1^\circ.5 \sim 200$ pc due to heavy extinction by bulge (Simion et al., 2017); hence, the major body of the bar is not observed.

The photometric scale radius of the disk of $a_4 \simeq 2.4$ kpc (Robin et al., 2014) is smaller than the present dynamical value of 3.9 kpc. However, the dynamical mass of $\sim 0.86 \times 10^{11} M_\odot$ is in good agreement with the current estimations from the literature (Bland-Hawthorn & Gerhard, 2016).

There seems to be no way to measure dark halo mass by photometry. Therefore, the dynamical fitting to RC up to ~ 300 kpc will be a powerful means to discuss the physics of the dark halo.

4.2 Implications of GRC on the Galactic dynamics

The rotation curve is defined as the mean circular velocity of gas and stars in the galactic plane as a one dimensional function of the radius R, where non-circular or non-axisymmetric properties, such as the east-west asymmetry of the terminal velocities with respect to the Galactic Center, have been averaged out. On this basis, we have obtained the approximate mass distribution in the Galaxy by deconvolving the curve into the five dynamical components, from the SMBC to the dark halo. Since it is a one variable function of R, a rotation curve cannot be used to directly calculate higher-order mass distributions, such as those due to a bar and spiral arms. Considering the effects of bar and spiral structures, there is a limitation on the use of the rotation curve, whereas it may assist in modeling the inner bar structure.

Evidence has accumulated that Galactic rotation contains non-axisymmetric components, with the amplitude depending on the galacto-centric distance. GAIA trigonometry revealed systematic non-circular motions of OB stars at $V_\phi - V_0 \sim \pm 5$ km s^{-1} in the Solar vicinity within ~ 2 kpc ($6.5 \lesssim R \lesssim 10$ kpc) due to the spiral arms (Gaia Collaboration et al., 2023). Since these motions of the arms are smaller than the errors of the present GRC of $\sim \pm 10$ km s^{-1} (table **??**) and are considered to be periodic (sinusoidal) from arm to arm, the GRC made from azimuthally averaged motions may be regarded as representing the circular motion within the errors attached in the table.

Eastern and western (positive and negative longitudes) asymmetry of the inner rotation curve at $R \lesssim 5$ kpc has long been known and is considered evidence of non-circular motion caused by a bar and/or spiral arms (Manabe & Miyamoto, 1975; Liszt & Burton, 1980; Sofue & Kohno, 2025). Our high-accuracy measurement of the terminal velocities of the CO and HI gas disks has revealed an east-to-west asymmetry at $R \lesssim 6$ km s^{-1} with the amplitude of ~ 20 km s^{-1} sinusoidally oscillating against R (Sofue & Kohno, 2025). A bar-induced eccentric flow has been more directly observed through the VLBI trigonometry of high-mass star masers, which has shown significant systematic non-circular motions of $\sim 30-50$ km s^{-1} near the Galactic bar end at $R \sim 5$ kpc ($3 \lesssim R \lesssim 5$ kpc) (Reid et al., 2019).

Given such a bar structure, the RC inside the central few kpc needs to be interpreted more carefully to see whether it explicitly reflects the dynamical mass or is affected by the eccentric motions, so that the RC derived value of the mass is under- or over-estimated compared to the true mass. Further discussion of a bar is beyond the scope of this paper, but a simulation-based study could be a possible tool to obtain the truth.

From the theoretical side, it is known that the bar-induced eccentric motion results in either an over- or under-estimation of the mass depending on the bar's position angle and pattern speed (Sorensen et al., 1976; Binney et al., 1991; Sormani et al., 2015a,b). Namely, bars with the same mass but different orientations yield different amplitudes and radii of the RC peak (Liu et al., 2025). In our Galaxy, this effect is typically observed as the high-velocity peak of the RC at $R \sim 0.4$ kpc.

Numerical simulations have shown that this RC peak can be explained by the streaming motion of gas in a nearly head-on bar (Chemin et al., 2015; Hunter et al., 2024; Sormani et al., 2015a,b; Baba, 2025). Therefore, the currently fitted bulge may not accurately reflect the actual mass structure. Conversely, the most accurate GRC presented in this paper, along with the well quantified E/W sinusoidal variation of the terminal velocity (Sofue & Kohno, 2025), can be used to validate the simulation results and constrain the parameters for the underlying mass model, including the bar's shape and mass distributions.

4.3 GRC27 as a template for observational constraint on theories

Thus far, the rotation curve is useful for wider purposes, not only for the estimation of the mass distribution but also for checking and constraining various theories and numerical simulations of Galactic stellar and gas dynamics. For this, we present the results in the Appendix as ASCII-formatted tables.

Table 2 lists the running average RC of the observed data presented in figure 1 within the disk inside $\sim$ 30 kpc and the raw values of $V_{3D}/\sqrt{2}$ for dwarf galaxies from the literature.

5 Summary

We derived the most completely sampled unified rotation curve of the Milky Way (GRC27), covering the widest radius from the central supermassive black hole to the outer halo of radius ~ 300 kpc, which has the highest resolution and accuracy ever achieved for a galaxy. The new curve will provide the most fundamental constraint on models and simulations of the structure and dynamics of the Galaxy.

As a trial, we decomposed the GRC into five components: the central black hole, the core, bulge, disk, and dark halo, and estimated their approximate scales and masses. The local dark matter density near the Sun, due to the dark halo alone, is estimated to be $\rho_\odot^{\rm DM} \sim 0.21$ GeV cm^{-3} . We found a linear proportionality between the scale radius and the mass of the individual components.

Acknowledgements

The computations were carried out at the Astronomy Data Center of the National Astronomical Observatory of Japan. The author acknowledges support from

JSPS KAKENHI Grant Number JP24H00004 and JP23K20035

Data availability

The GRC27 obtained here is listed in the tables in the Appendix.

Conflict of interest

The author has no conflict of interest.

References

2025ApJ...989..121B Baba, J. 2025, ApJ, 989, 1, 121.

Binney, J., Gerhard, O. E., Stark, A. A., et al. 1991, MNRAS, 252, 210.

Bird, S. A., Xue, X.-X., Liu, C., et al. 2022, MNRAS, 516, 1, 731.

Bland-Hawthorn, J. & Gerhard, O. 2016, ARA&A, 54, 529.

Braiding, C., Burton, M. G., Blackwell, R., et al. 2015, PASA, 32, e020.

Chemin, L., Renaud, F., & Soubiran, C. 2015, A$A, 578, A14.

Cubuk, K. O., Burton, M. G., Braiding, C., et al. 2023, PASA, 40, e047.

Dame, T. M., Hartmann, D., & Thaddeus, P. 2001, ApJ, 547, 2, 792.

Eadie, G. & Jurić, M. 2019, ApJ, 875, 2, 159.

Eilers, A.-C., Hogg, D. W., Rix, H.-W., et al. 2019, ApJ, 871, 1, 120.

Einasto, J. 1965, Trudy Astrofizicheskogo Instituta Alma-Ata, 5, 87.

Freeman, K.C. On the Disks of Spiral and S0 Galaxies. Astrophys. J. 1970, 160, 811.

Gaia Collaboration, Drimmel, R., Romero-Gómez, M., et al. 2023, A&A, 674, A37.

GRAVITY Collaboration, Abuter, R., Aimar, N., et al. 2022, A&A, 657, L12.

Gravity Collaboration, Abuter, R., Amorim, A., et al. 2019, A&A, 625, L10.

Hammer, F., Wang, J., Pawlowski, M. S., et al. 2021, ApJ, 922, 2, 93.

Hammer, F., Li, H., Mamon, G. A., et al. 2023, MNRAS, 519, 4, 5059.

HI4PI Collaboration, Ben Bekhti, N., Flöer, L., et al. 2016, A&A, 594, A116.

Huang, Y., Liu, X.-W., Yuan, H.-B., et al. 2016, MNRAS, 463, 3, 2623.

Hunter, G. H., Sormani, M. C., Beckmann, J. P., et al. 2024, A&A, 692, A216.

Iocco, F.; Pato, M.; Bertone, G.Nat. Phys. 2015, 11, 245.

Jiao, Y., Hammer, F., Wang, H., et al. 2023, A&A, 678, A208.

Kormendy, J. & Ho, L. C. 2013, ARA&A, 51, 1, 511.

Lelli, F., McGaugh, S. S., & Schombert, J. M. 2016, AJ, 152, 6, 157.

Li, Z.-Z.; Jing, Y.P.; Qian, Y.-Z.; Yuan, Z.; Zhao, D.-H. ApJ 2017, 850, 116.

Li, H., Hammer, F., Babusiaux, C., et al. 2021, ApJ, 916, 1, 8.

Liu, J., Li, Z., & Shen, J. 2025, ApJ, 980, 1, 146.

Liszt, H. S. & Burton, W. B. 1980, ApJ, 236, 779.

Longmore, S. N., Bally, J., Barnes, A. T., et al. 2026, MNRAS, 552, 2, stag377. doi:10.1093/mnras/stag377

McGaugh, S. S. 2016, ApJ, 816, 1, 42.

Manabe, S. & Miyamoto, M. 1975, PASJ, 27, 1, 35.

Marasco, A., Fall, S. M., Di Teodoro, E. M., et al. 2025, A&A, 695, L23.

Navarro, J.F.; Frenk, C.S.; White, S.D.M.ApJ. 1997, 490, 493.

Nelson, A. H., Sofue, Y., & Williams, P. R. 2026, A&A, 713, A339.

Ness, M. & Lang, D. 2016, AJ, 152, 1, 14.

Ou, X., Eilers, A.-C., Necib, L., et al. 2024, MNRAS, 528, 1, 693.

Portail, M., Wegg, C., Gerhard, O., et al. 2015, MNRAS, 448, 1, 713.

Reid, M. J., Menten, K. M., Brunthaler, A., et al. 2019, ApJ, 885, 2, 131.

Retana-Montenegro, E., van Hese, E., Gentile, G., et al. 2012, A&A, 540, A70. doi:10.1051/0004-6361/201118543

Robin, A. C., Marshall, D. J., Schultheis, M., et al. 2012, A&A, 538, A106.

Robin, A. C., Reylé, C., Fliri, J., et al. 2014, A&A, 569, A13.

Salomon, J.-B., Ibata, R. A., Famaey, B., et al. 2016, MNRAS, 456, 4, 4432. doi:10.1093/mnras/stv2865

Salucci, P.A&Ap. Rev. 2019, 27, 2.

Schödel, R., Feldmeier, A., Kunneriath, D., et al. 2014, A&A, 566, A47.

Simion, I. T., Belokurov, V., Irwin, M., et al. 2017, MNRAS, 471, 4, 4323.

Sofue, Y. 2012, PASJ, 64, 75.

Sofue, Y. PASJ 2013, 65, 118.

Sofue, Y.PASJ 2017, 69, R1.

Sofue, Y. 2020, Galaxies, 8, 37.

Sofue, Y.; Honma, M.; Omodaka, T. PASJ 2009, 61, 227.

Sofue, Y. & Kohno, M. 2025, PASJ, 77, 6, 1335.

Sofue, Y., Oka, T., Longmore, S. N., et al. 2025, arXiv:2504.03331.

Sofue, Y.; Rubin, V.ARA&Ap 2001, 39, 137.

Sorensen, S.-A., Matsuda, T., & Fujimoto, M. 1976, Ap&SS, 43, 2, 491.

Sormani, M. C., Binney, J., & Magorrian, J. 2015, MNRAS, 449, 3, 2421.

Sormani, M. C., Binney, J., & Magorrian, J. 2015, MNRAS, 454, 2, 1818.

Sylos Labini, F. 2024, ApJ, 976, 2, 185.

Umemoto, T., Minamidani, T., Kuno, N., et al. 2017, PASJ, 69, 78

Valenti, E., Zoccali, M., Gonzalez, O. A., et al. 2016, A&A, 587, L6.

VERA Collaboration, Hirota, T., Nagayama, T., et al. 2020, PASJ, 72, 4, 50.

Wegg, C., Gerhard, O., & Portail, M. 2015, MNRAS, 450, 4, 4050.

Vasiliev, E. & Baumgardt, H. 2021, MNRAS, 505, 4, 5978.

Wang, J., Hammer, F., & Yang, Y. 2022, MNRAS, 510, 2, 2242.

White, M. 2001, A&A, 367, 27.

Zhou, Y., Li, X., Huang, Y., et al. 2023, ApJ, 946, 2, 73.

A Table of the rotation curve of the Milky Way

We present the GRC27 in ASCII formatted tables in table 2.

Table 2 Running averated rotation curve of the Milky Way

R (pc)	V (km s^{-1})	δV (km s^{-1})	R (pc)	V (km s^{-1})	δV (km s^{-1})	R (pc)	V (km s^{-1})	δV (km s^{-1})
0.108E+00	416.9	15.1	0.363E+02	89.8	9.6	0.122E+05	226.2	3.0
0.119E+00	397.5	14.4	0.399E+02	94.6	6.6	0.134E+05	224.4	2.6
0.131E+00	379.0	13.7	0.439E+02	95.4	5.8	0.147E+05	221.6	2.9
0.144E+00	361.3	13.2	0.483E+02	93.2	5.5	0.162E+05	218.7	2.8
0.159E+00	344.4	12.7	0.531E+02	90.2	5.0	0.178E+05	215.1	4.1
0.175E+00	328.4	11.9	0.584E+02	92.8	6.7	0.196E+05	209.1	6.0
0.192E+00	313.2	11.3	0.643E+02	97.4	7.9	0.215E+05	204.4	5.9
0.211E+00	298.6	10.7	0.707E+02	105.1	13.4	0.237E+05	201.8	9.9
0.232E+00	284.7	10.2	0.778E+02	114.6	14.0	0.260E+05	195.1	24.1
0.255E+00	271.5	9.8	0.856E+02	107.7	13.4	0.287E+05	186.4	34.8
0.281E+00	258.9	9.4	0.941E+02	97.3	7.9	0.315E+05	183.7	35.9
0.309E+00	246.8	8.9	0.104E+03	94.7	6.5	0.347E+05	194.2	33.4
0.340E+00	235.3	8.5	0.114E+03	96.2	9.0	0.382E+05	205.3	17.3
0.374E+00	224.4	8.1	0.125E+03	96.8	12.8	0.420E+05	195.6	14.3
0.411E+00	213.9	7.7	0.138E+03	97.8	17.8	0.462E+05	177.5	17.5
0.453E+00	203.8	8.2	0.152E+03	121.2	20.4	0.508E+05	172.4	17.0
0.498E+00	194.2	9.0	0.167E+03	138.5	7.2	0.558E+05	156.1	31.9
0.548E+00	187.7	6.5	0.183E+03	145.2	5.0	0.614E+05	123.1	24.0
0.602E+00	185.5	3.8	0.202E+03	155.8	17.1	0.676E+05	125.0	22.7
0.663E+00	184.3	3.2	0.222E+03	196.9	28.5	0.743E+05	130.5	21.4
0.729E+00	176.9	6.6	0.244E+03	220.7	13.1	0.818E+05	148.5	23.6
0.802E+00	166.0	6.7	0.268E+03	224.9	6.3	0.899E+05	154.8	24.2
0.882E+00	143.3	25.8	0.295E+03	219.8	8.1	0.989E+05	128.0	33.0
0.970E+00	115.7	12.7	0.325E+03	224.7	13.4	0.109E+06	111.2	30.0
0.107E+01	121.0	14.6	0.357E+03	243.3	11.7	0.120E+06	104.1	24.3
0.117E+01	131.6	14.8	0.393E+03	251.9	4.9	0.132E+06	95.4	18.3
0.129E+01	130.0	13.8	0.432E+03	253.2	1.9	0.145E+06	90.0	18.4
0.142E+01	120.0	10.1	0.476E+03	255.1	1.4	0.159E+06	84.7	20.0
0.156E+01	117.7	9.5	0.523E+03	255.6	0.7	0.175E+06	85.5	25.5
0.172E+01	117.1	10.3	0.576E+03	254.7	2.2	0.193E+06	77.7	15.7
0.189E+01	116.1	7.3	0.633E+03	250.5	5.5	0.212E+06	74.5	8.1
0.208E+01	116.3	6.8	0.696E+03	242.7	5.3	0.233E+06	102.5	32.1
0.229E+01	113.1	10.4	0.766E+03	236.4	7.4	0.257E+06	126.7	16.8
0.252E+01	112.6	13.4	0.843E+03	226.9	9.6	0.282E+06	130.1	8.2
0.277E+01	105.4	13.7	0.927E+03	212.7	8.3	0.000E+00	0.0	0.0
0.305E+01	102.0	10.1	0.102E+04	206.9	3.7	0.000E+00	0.0	0.0